

# Mixing-Denoising Generalizable Occupancy Networks

Amine Ouasfi      Adnane Boukhayma  
Inria, Univ. Rennes, CNRS, IRISA, M2S, France

## Abstract

While current state-of-the-art generalizable implicit neural shape models [7, 54] rely on the inductive bias of convolutions, it is still not entirely clear how properties emerging from such biases are compatible with the task of 3D reconstruction from point cloud. We explore an alternative approach to generalizability in this context. We relax the intrinsic model bias (i.e. using MLPs to encode local features as opposed to convolutions) and constrain the hypothesis space instead with an auxiliary regularization related to the reconstruction task, i.e. denoising. The resulting model is the first only-MLP locally conditioned implicit shape reconstruction from point cloud network with fast feed forward inference. Point cloud borne features and denoising offsets are predicted from an exclusively MLP-made network in a single forward pass. A decoder predicts occupancy probabilities for queries anywhere in space by pooling nearby features from the point cloud order-invariantly, guided by denoised relative positional encoding. We outperform the state-of-the-art convolutional method [7] while using half the number of model parameters.

## 1. Introduction

One of the most sought after goals in modern day computer vision and machine learning is enabling machines to understand and navigate 3D given limited input. This faculty is manifested in several downstream vision and graphics tasks, such as shape reconstruction from noisy and relatively sparse point clouds. Recovering full shape from point clouds is all the more an important problem in account of the ubiquity of this light, albeit incomplete, 3D representation, whether it is acquired from the nowadays increasingly accessible scanning devices, or as obtained from multi-view vision algorithms such as Structure From Motion or Multi-View Stereo (e.g. [63, 64]). While classical optimization based approaches such as Poisson Reconstruction [33] or moving least squares [28] can mostly successfully deliver from dense clean point sets and normal estimations, the deep learning based more recent alternatives offer faster and more robust prediction especially for noisy and sparse in-

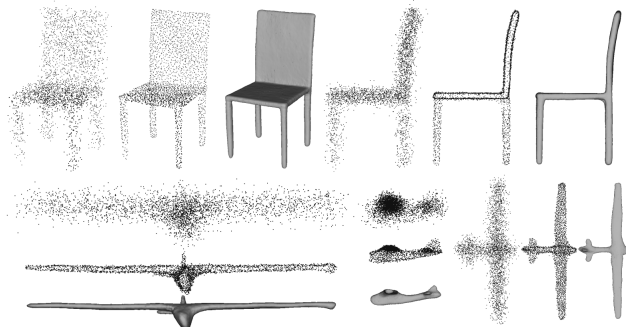


Figure 1. Our method couples 3D implicit reconstruction with explicit denoising of point clouds. We show here reconstruction examples from 3000 noisy points (Gaussian noise of std. dev. 0.025). We show the input, our intermediate denoised point cloud, and our predicted geometry.

puts, without requiring normals.

For learning based reconstruction from point cloud, feed forward (optimization-free) generalizable models are important to the community by virtue of their high performances and fast inference. State-of-the-art ones are based on implicit neural shape representations. Typically [15, 54], a deep convolutional network builds features from the input point cloud, then an implicit decoder maps the feature of a query point to its occupancy or signed distance w.r.t. the target shape. While the ConvNet predicts explicit extrinsic features in [15, 54, 55], recent work [7] suggests that learning features intrinsically *i.e.* only at the point cloud yields superior results. In this case, features for query points are pooled from the nearest points of the input point cloud.

While the aforementioned existing work advocates using convolutions to achieve generalizability for this problem, we ask our selves the question, what if we do not constrain our hypothesis space in such an Ad hoc way ? *i.e.* what if we use the most inductive bias free model possible, and rely on supervision and eventually regularizations, would we succeed in achieving generalization while maintaining fast inference ? This line of thought is inspired by the recent success of MLP-only models in vision [72] and their application to point cloud processing [17]. Their idea consists in applying MLPs (mixing) to the data feature dimension

and the spatial dimension separately and repeatedly. Point clouds being unordered and irregular, the spatial (Token) mixing is achieved with an order-invariant (Softmax) based pooling on a limited support from the point cloud.

Based on all the above, we propose a new encoder-decoder model for implicit reconstruction from point cloud. It processes the input point cloud intrinsically (as in [7]) but uses solely MLPs from start to end (unlike [7]). This allows us to outperform the state-of-the-art method [7] whilst using only half the number of parameters (6.5M for us, vs. 12.5M for [7]). Not only this shows that convolution inductive biases are not a necessity in this context, but we even achieve a more parameter efficient intrinsic point cloud reconstruction model without them. Additionally, we show that coupling our implicit reconstruction learning with a related regularization task, in the form of weakly supervised point cloud denoising, can yield even better generalization. In fact, the performance gap between our method trained with and without denoising increases fourfold in Chamfer distance, when going to a setup requiring more generalization ability (See intra-ShapeNet generalization in Table 2, vs. the more challenging ShapeNet to ScanNet generalization in Table 5).

Our network builds on the dense task prediction model PointMixer [17] to predict per-point features. However, to infer occupancies for extrinsic query points (not only on the point cloud), we introduce the new "Extra-set" mixing layer in concordance with PointMixer terminology. The "Extra-set" mixing layer pools features from nearby points of the input point cloud. As this pooling can be guided with positional encoding of the query relative to these support points, we task our PointMixer additionally with denoising the point cloud in parallel, and we use the denoised point cloud to compute more accurate positional encodings (unlike [7]). Furthermore, differently from [7], we incorporate a global decoder using coarse features on a downsampled point cloud as pooling support, in order to robustify the method against local outliers.

We note that existing MLP-only feed forward generalizable methods lack a local feature aggregation mechanism in their encoder architectures (PointNet), which is crucial for performance without sacrificing inference speed. [48] used a global feature causing under-performance. [22] enforces locality through query point dependent local patch inputs, hence requiring as many encoder forward passes as there are query points. This naturally results in significantly increased inference times surpassing even *e.g.* some auto-decoding optimization based methods. Conversely, being equipped with point mixing locality, our MLP-only model's encoder solely requires a single pass for the input point cloud. It offers consequently about 3 orders of magnitude faster reconstruction (within 500ms at resolution  $128^3$ ) compared to [22], in line with convolutional locality

endowed competitors ([7, 54]).

We outperform existing comparable methods on standard benchmarks for object and scene level reconstruction, and in generalization to real scan data (Section 4). The performance gap is most important in the most sparse and noisy input setup (Table 1), demonstrating our resilience to scarcity and corruption. Our reconstructions are also more robust, as witnessed by our superior L2 Chamfer errors across all benchmarks. We evaluate the benefits of each of our contributions in our ablation section (4.7).

Our contributions can be summarized as follows:

- A convolution-free feed forward intrinsic occupancy network from point cloud attaining the new state-of-art, while being twice as parameter efficient as its closest intrinsic convolutional counterpart ([7]).
- Joint learning of implicit reconstruction from point cloud with explicit point cloud denoising for the first time to the best of our knowledge.
- Combining local and global pooling based decoding for deep intrinsic (*e.g.* [7]) occupancy regression.

## 2. Related work

**Shape Representations in Deep Learning** Shapes can be represented in deep learning either intrinsically or extrinsically. Intrinsic representations discretize the shape itself. When done explicitly using *e.g.* tetrahedral or polygonal meshes [32, 76], or point clouds [23], this bounds the output topology thus limiting the variability of outputs. Among other forms of intrinsic representations, 2D patches [21, 27, 80] can prompt discontinuities, whilst the simple nature of shape primitives such as cuboids [74, 92], planes [39] and Gaussians [24] limits their expressivity. Differently, extrinsic shape representations model the space containing the scene/object. Voxel grids [84, 85] are the most popular one being the extension of 2D pixels to 3D domain. Their capacity is limited though by their cubic resolution memory cost. Sparse representation like octrees [60, 71, 78] can alleviate this issue to some extent.

**Implicit Neural Shape Representations** Implicit neural representations (INRs) stood out as a major new medium for modelling shape and radiance (*e.g.* [11, 30, 49, 77, 86]) extrinsically. They overcome many of the limitations of the aforementioned classical representations thanks to their ability to represent shapes with arbitrary topologies at virtually infinite resolution. They are usually parameterised with MLPs mapping spatial locations or features to *e.g.* occupancy [48], signed [53] or unsigned [16, 91] distances relative to the target shape. The level-set of the inferred field from these MLPs can be rendered through ray marching [29], or tessellated into an explicit shape using *e.g.* Marching Cubes [43]. A noteworthy branch of work builds hy-

brid implicit/explicit representations [14, 20, 52, 87] based mostly on differentiable space partitioning.

### Generalizing Implicit Neural Shape Representations

In order to represent collections of shape, implicit neural models require conditioning mechanisms. These include latent code concatenation, batch normalization, hypernetworks [65, 67, 68, 79] and gradient-based meta-learning [50, 66]. Concatenation based conditioning was first implemented using single global latent codes [13, 48, 53], and further improved with the use of local features [15, 22, 25, 31, 35, 54, 69, 73].

**Shape Reconstruction from Point Cloud** Classical approaches include combinatorial ones where the shape is defined through an input point cloud based space partitioning, through *e.g.* alpha shapes [5] Voronoi diagrams [1] or triangulation [9, 41, 59]. On the other hand, the input samples can be used to define an implicit function whose zero level set represents the target shape, using global smoothing priors [36, 81, 82] *e.g.* radial basis function [8] and Gaussian kernel fitting [62], local smoothing priors such as moving least squares [28, 34, 42, 47], or by solving a boundary conditioned Poisson equation [33]. The recent literature proposes to parameterise these implicit functions with deep neural networks and learn their parameters with gradient descent, either in a supervised or unsupervised manner.

**Unsupervised Implicit Neural Reconstruction** A neural network is typically fitted to the input point cloud without extra information. Regularizations can improve the convergence such as the spatial gradient constraint based on the Eikonal equation introduced by Gropp *et al.* [26], a spatial divergence constraint as in [4], Lipschitz regularization on the network [40]. Atzmon *et al.* learn an SDF from unsigned distances [2], and further supervises the spatial gradient of the function with normals [3]. Ma *et al.* [44] expresses the nearest point on the surface as a function of the neural signed distance and its gradient. They also leverage self-supervised local priors to deal with very sparse inputs [45] and improve generalization [46]. All of the aforementioned work benefits from efficient gradient computation through back-propagation in the neural network. Periodic activations were introduced in [67]. Lipman [38] learns a function that converges to occupancy while its log transform converges to a distance function. [81] learns infinitely wide shallow MLPs as random feature kernels.

**Supervised Implicit Neural Reconstruction** Supervised methods assume a labeled training data corpus commonly in the form of dense samples with ground truth shape information. Auto-decoding methods [10, 31, 35, 53, 73]

require test time optimization to be fitted to a new point cloud, which can take up to several seconds. Encoder-decoder based methods enable fast feed forward inference. Introduced first in this respect, Pooling-based set encoders [13, 25, 48] such as PointNet [56] have been shown to underfit the context. Convolutional encoders yield state-of-the-art performances. They use local features either defined in explicit volumes and planes [15, 37, 54, 55] or solely at the input points [7]. Ouasfi and Boukhayma [51] proposed concurrently to robustify the generalization of these models through transfer learning to a kernel ridge regression whose hyperparameters are fitted to the shape. Peng *et al.* [55] proposed a differentiable Poisson solving layer that converts predicted normals into an indicator function grid efficiently. However, it is limited to small scenes due to the cubic memory requirement in grid resolution.

## 3. Method

Given a noisy input point cloud  $\mathbf{X} \subset \mathbb{R}^{N_p \times 3}$ , our objective is to recover a shape surface  $\mathcal{S}$  that best explains this observation, *i.e.* the input point cloud elements being noisy samples from  $\mathcal{S}$ .

To achieve this, we train a deep implicit neural network  $f_\theta$  to predict occupancy values relative to a target shape  $\mathcal{S}$  at any queried Euclidean space location  $x \in \mathbb{R}^3$ , given the input point cloud  $\mathbf{X}$ , *i.e.*  $f_\theta(\mathbf{X}, x) = 1$  if  $x$  is inside, and 0 otherwise. The inferred shape  $\hat{\mathcal{S}}$  can then be obtained as a level set the occupancy field inferred using  $f_\theta$ :

$$\hat{\mathcal{S}} = \{x \in \mathbb{R}^3 \mid f_\theta(\mathbf{X}, x) = 0.5\}. \quad (1)$$

In practice, an explicit triangle mesh for  $\hat{\mathcal{S}}$  is extracted using the Marching Cubes [43] algorithm.

We opt for a feed forward conditional implicit model  $f_\theta$ , as we want our method to generalize to multiple shapes simultaneously and provide fast test-time optimization free inference. Similarly to the state-of-the-art in this category *e.g.* [7, 54],  $f_\theta$  consists of a point cloud conditioning network and an implicit decoder.

### 3.1. Model

The staple back-bone model for feed-forward generalizable 3D shape reconstruction from point cloud has lately been the one introduced by Peng *et al.* [54], which also bears similarities with the concurrent work by Chibane *et al.* [15]. It has been widely used among methods predicting other implicit fields from point clouds as well, such as point displacements [75], unsigned distances [16] or whether point pairs are separated by a surface [88]. In this model, the encoder builds an explicit extrinsic 3D feature volume from the voxelized or pixelized input point cloud through 3D (or 2D) convolutional networks.

Recently, Boulch *et al.* [7] argued against this strategy. They contented that these methods operate in a voxelized

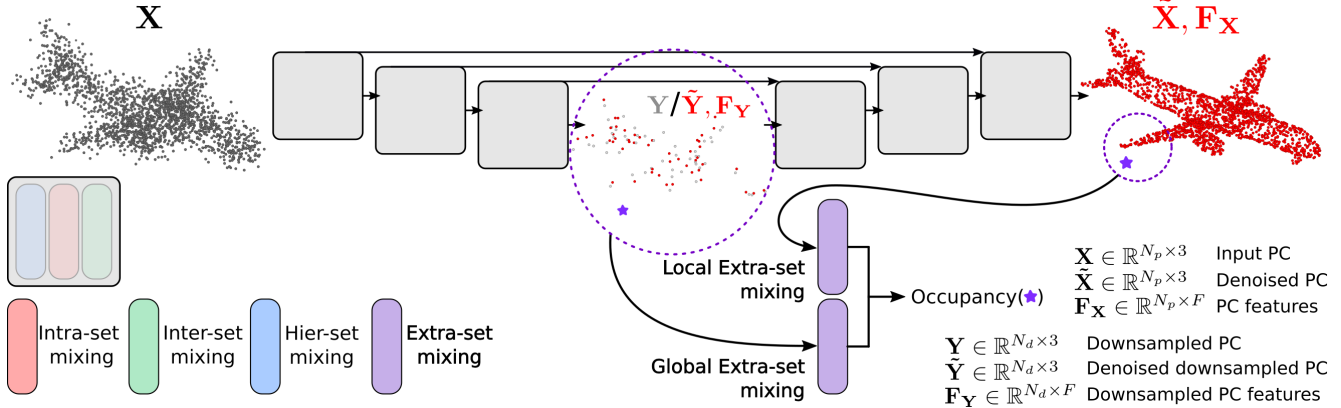


Figure 2. Overview: Our method uses exclusively MLPs from beginning to end to predict an implicit shape function given a noisy input point cloud. First a U-Net PointMixer [17] (Gray boxes) is tasked with denoising the input and producing per point features. The building blocks of this network combine 3 pre-existing forms of point mixing which pool features from support points in a point cloud into other points of the point cloud. Channel-wise mixing is also used throughout the model as well. We refer the reader to the work of Choe *et al.* [17] for a detailed description on these preexisting mixing layers. We introduce "Extra-set mixing" (Section 3.3), which we use to pool features both locally and globally onto any external query point to estimate its occupancy. This mixing is guided by relative positional encoding using the denoised support point coordinates (See Figure 3).

discretization whose voxel centers maybe far from the input point cloud locations. They also argued that voxel centers holding the shape information are uniformly sampled, while they should be ideally more focused near the surface. Conclusively, they introduced a point cloud convolutional encoder, where features are only defined at the input point cloud locations, where shape information matters most. They achieve superior reconstruction performances consequently on several benchmarks.

Both of the aforementioned strategies however still rely on convolutions for translational equivariance and generalization across scenes and objects. Differently, we propose here an architecture based solely on MLPs, and show that it mostly outperforms the previously mentioned strategies.

### 3.2. Feature Extraction and Denoising Network

Our point cloud feature extraction network takes noisy point cloud  $\mathbf{X}$  as input and produces an output per element in the point cloud. However, differently from [7], it does not use convolutions, but bases the entire model on MLPs instead, inspired by recent success of the PointMixer [17] architecture.

Specifically, we use the dense prediction task model in [17], which consists of a U-Net [61] symmetric encoder-decoder scheme. The point cloud is downsampled gradually throughout the encoder  $E$  using Farthest point sampling until it reaches the coarsest point cloud  $\mathbf{Y} \in \mathbb{R}^{N_d \times 3}$ . It is upsampled back then correspondingly through out the decoder  $D$ . As illustrated in Figure 2, each block in the encoder/decoder consists mostly of a Hierarchical mixing layer, an intra-set mixing layer, a inter-set mixing layer and

channel mixing, as elaborated in [17].

The channel mixing layer is an MLP operating directly on the feature domain, *i.e.* mixing feature channels. The other mixings are point-wise mixings to replace the token-wise mixing in the original MLP-Mixer model [72]. They are softmax based order invariant pooling layers, that pool features from a limited set of point cloud support points into a point cloud query. They vary in the way their supports are defined. In the intra-set one the support is the nearest points to the query. In the inter-set one the support is the inverse of the intra-set support, *i.e.* a point is part of the support of a query if the query is part of the nearest points of that point. The hierarchical-set mixing is used for down/up transitions in the encoder/decoder, and hence the support is the nearest points in the previous/next point cloud resolution. In practice, for the decoder to be symmetrical with the encoder, the up transition support set is defined as the inverse of the equivalent down transition support set, differently from seminal work [57, 89, 90]. For a more thorough explanation of the intra-set, inter-set and hierarchical-set mixing layers we refer the reader to the work by Choe *et al.* [17].

Differently from [7], we design our feature extraction network to perform two tasks simultaneously: produce per point fine features  $\mathbf{F}_X \in \mathbb{R}^{N_p \times F}$  and displacement vectors  $\Delta \mathbf{X} \in \mathbb{R}^{N_p \times 3}$ :

$$\mathbf{F}_X, \Delta \mathbf{X} = D \circ E(\mathbf{X}). \quad (2)$$

We train the displacements semi-supervisedly to produce a denoised version  $\tilde{\mathbf{X}} \in \mathbb{R}^{N_p \times 3}$  of the input point cloud:

$$\tilde{\mathbf{X}} = \mathbf{X} + \Delta \mathbf{X}. \quad (3)$$



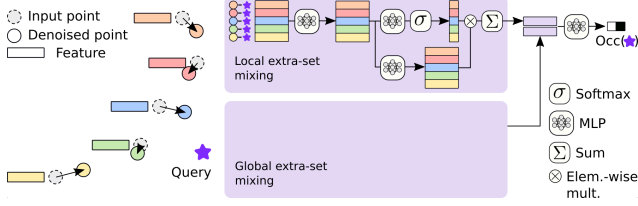


Figure 3. Using denoised point coordinates and features, our implicit decoder performs local and global extra-set point mixing at a given query location to predict its shape occupancy value. The global extra-set mixing mechanism is similar to the local one. The local extra-set mixing uses the  $K$  nearest denoised points of the point cloud. The global extra-set mixing uses the full  $N_d$  denoised points of the downsampled point cloud.

We note that using the encoder  $E$ , we can also extract coarse features  $\mathbf{F}_Y$  for the downsampled point cloud  $Y$  at the bottleneck of the model:

$$\mathbf{F}_Y = E(\mathbf{X}). \quad (4)$$

A denoised version  $\tilde{\mathbf{Y}} \in \mathbb{R}^{N_d \times 3}$  of the downsampled input point cloud  $Y$  can be naturally obtained from the output denoised point cloud  $\tilde{\mathbf{X}}$  via the encoder defined downsampling indexing  $\delta: \llbracket 1, N_p \rrbracket \rightarrow \llbracket 1, N_d \rrbracket$ :

$$\tilde{\mathbf{Y}}_i = \tilde{\mathbf{X}}_{\delta(i)}, \quad \mathbf{Y}_i = \mathbf{X}_{\delta(i)}. \quad (5)$$

### 3.3. Extra-set Mixing Decoder

To serve the role of our implicit decoder, we introduce a new point mixing layer, borrowing the terminology in Point-Mixer [17]. As opposed to the existing point mixing layers in [17], this layer takes as input a query point representing any location in Euclidean space, and not necessarily an element from the input point cloud topology  $\mathbf{X}$ , hence the denomination "Extra-set". Similarly to the point-mixing layers in [17], it pools features from a support set using softmax in an order-invariant fashion.

We first use our layer to extract a local fine feature  $\mathbf{y}^{loc}$  for a query point  $q \in \mathbb{R}^3$ . This feature is built using the  $K$  nearest points to  $q$  from the denoised output point cloud  $\tilde{\mathbf{X}}$  and their corresponding output fine features in  $\mathbf{F}_X$ , as generated by decoder  $D$ .

To this end, and as illustrated in Figure 3, we first compute an aggregation score  $s_{\tilde{p}}$  for each support element  $\tilde{p}$ :

$$s_{\tilde{p}} = g_2 \circ g_1(\tilde{p} - q; \mathbf{F}_X(p)), \quad \tilde{p} \in \mathcal{X}_q = k\text{NN}(\tilde{\mathbf{X}}, q), \quad (6)$$

where  $g_1(\cdot)$  and  $g_2(\cdot)$  are channel mixing MLPs and  $\mathbf{F}_X(p)$  is the fine feature of denoised support point  $\tilde{p}$ . We use these aggregation scores to pool features of the support points into the final local feature of the query point:

$$\mathbf{y}^{loc} = \sum_{\tilde{p} \in \mathcal{X}_q} \text{softmax}(s_{\tilde{p}}) \odot [g_3 \circ g_1(\tilde{p} - q; \mathbf{F}_X(p))], \quad (7)$$

where  $\text{softmax}(\cdot)$  is the softmax normalization over the support point dimension,  $g_3(\cdot)$  is another channel mixing MLP, and  $\odot$  denotes the element wise product. Conclusively, this layer is in fact akin to a spatial attention module [83], space here spanning the support points.

We note additionally that the architecture of this layer follows the decoder in [7]. Most importantly, we pinpoint that a main difference here is that the relative positional encoding in our extra-set mixing uses denoised support coordinates:  $\{\tilde{p} - q\}$ ,  $\tilde{p} \in \tilde{\mathbf{X}}$ , instead of the original noisy ones:  $\{p - q\}$ ,  $p \in \mathbf{X}$ , as done in [7]. This allows us to reduce the effect of noise on the Euclidean relative position guided feature aggregation. Similarly to [7], we use in practice  $N_H$  MLPs  $g_2$  in parallel, *i.e.*  $\text{softmax}(s_{\tilde{p}}) := \frac{1}{N_H} \sum_{h=1}^{N_H} \text{softmax}(g_2^h \circ g_1(\tilde{p} - q; \mathbf{F}_X(p)))$ .

Next, we use our layer introduced above to extract a global coarse feature  $\mathbf{y}^{glob}$  as well for a query point  $q \in \mathbb{R}^3$ . The goal of this global mixing component is to include global context in the reconstruction task and prevent the method from over-fitting on local information. This feature is built using the entire  $N_d$  sized down-sampled denoised point cloud  $\tilde{\mathbf{Y}}$  elements, along with their corresponding output coarse features in  $\mathbf{F}_Y$ , as generated by encoder  $E$ .

Similarly to the previous case, we first compute aggregation scores  $r_{\tilde{p}}$  for each support element  $\tilde{p}$ , and we use a support point-wise softmax normalization of these scores to weight the support point features:

$$r_{\tilde{p}} = h_2 \circ h_1(\tilde{p} - q; \mathbf{F}_Y(\tilde{p})), \quad \tilde{p} \in \tilde{\mathbf{Y}}. \quad (8)$$

$$\mathbf{y}^{glob} = \sum_{\tilde{p} \in \tilde{\mathbf{Y}}} \text{softmax}(r_{\tilde{p}}) \odot [h_3 \circ h_1(\tilde{p} - q; \mathbf{F}_Y(\tilde{p}))], \quad (9)$$

where  $h_1(\cdot)$ ,  $h_2(\cdot)$  and  $h_3(\cdot)$  are channel mixing MLPs, and  $\mathbf{F}_Y(p)$  is the coarse feature of denoised support point  $\tilde{p}$ .

Finally, a last channel mixing MLP  $g_4(\cdot)$  combines the local feature  $\mathbf{y}^{loc}$  and the global feature  $\mathbf{y}^{glob}$  of a query point  $q$  to produce the occupancy probability of the latter, which writes:

$$f_{\theta}(\mathbf{X}, q) := \text{occ}(q) = g_4(\mathbf{y}^{loc}; \mathbf{y}^{glob}). \quad (10)$$

### 3.4. Training

Our method is fully differentiable and is trained end-to-end leveraging the combination of a reconstruction loss and a denoising loss:

$$\mathcal{L} = \mathcal{L}_{\text{rec}} + \mathcal{L}_{\text{den}}. \quad (11)$$

We train the feature extraction and denoising network to produce a denoising offset for each input point by back-propagating the L2 Chamfer distance between the denoised point cloud  $\tilde{\mathbf{X}}$  and a ground truth point cloud sampled from

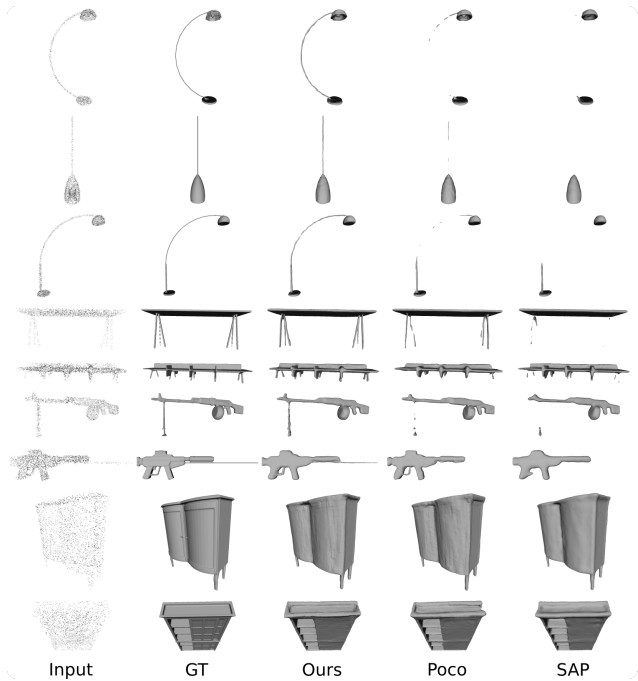


Figure 4. ShapeNet reconstructions from 3000 noisy points, with standard deviation of 0.005. Our method reproduces details and fine structures with more fidelity.

the ground truth shape  $\mathbf{X}_{\text{gt}} \sim \mathcal{S}$ :

$$\mathcal{L}_{\text{den}} = \frac{1}{2|\tilde{\mathbf{X}}|} \sum_{\tilde{p} \in \tilde{\mathbf{X}}} \min_{p \in \mathbf{X}_{\text{gt}}} \|p - \tilde{p}\|_2^2 + \frac{1}{2|\mathbf{X}_{\text{gt}}|} \sum_{p \in \mathbf{X}_{\text{gt}}} \min_{\tilde{p} \in \tilde{\mathbf{X}}} \|p - \tilde{p}\|_2^2, \quad (12)$$

where  $|\cdot|$  is the point set cardinality. A similar loss is used in recent supervised point cloud denoising literature (e.g. [58]). Ground truth point cloud  $\mathbf{X}_{\text{gt}}$  counts 100k ground truth surface samples. Besides providing more accurate support relative positional encoding for the decoder extra-set mixing, this loss can provide additional regularization to the feature extraction network, due to the correlations between the denoising and reconstruction tasks.

Following seminal work [48], the reconstruction loss is the Binary Cross-entropy loss between query points  $\{q\}$  sampled around the ground truth surface  $\mathcal{S}$  and their ground truth occupancy labels:

$$\mathcal{L}_{\text{rec}} = \sum_q \text{BCE}(\text{occ}(q), \text{occ}(q)_{\text{gt}}). \quad (13)$$

## 4. Results

We compare in this section our approach quantitatively and qualitatively to state-of-the-art methods on object and scene reconstruction benchmarks, using both synthetic and real data.

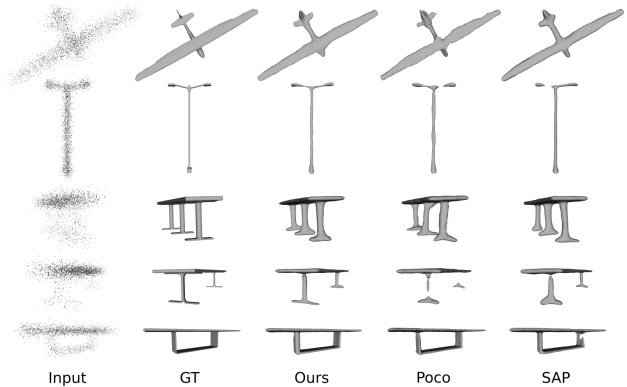


Figure 5. ShapeNet reconstructions from 3000 noisy points, with standard deviation of 0.025. We show more resilience to high levels of noise.

### 4.1. Implementation details

We implement our method using the PyTorch Framework. The U-Net follows the architecture in [17]. Coarse and fine feature dimensions are  $F_c = 512$  and  $F_f = 32$  respectively. For inputs of size  $N_p = 3000$ , we use  $N = 64$  nearest neighbor as the local decoder support size. For  $N = 300$ ,  $N = 12$ . The downsampled point cloud is of size  $N_d = 12$ . MLPs  $g_1/h_1$  have 3 ReLU activated hidden layers of dimension 32.  $g_2/h_2$  and  $g_3/h_3$  have one layer of dimension 64 and 32 respectively.  $g_4$  has two layers of dimensions 64 and 2.  $N_H = 64$ . Following [7], we train for 600k iterations in batches of 16 shapes and 2048 query points, and we reconstruct similarly at resolution 256.

### 4.2. Metrics

Following seminal work, we evaluate our method and the competition w.r.t. the ground truth using standard metrics for the 3D reconstruction task. Namely, the L1 and L2 Chamfer Distances  $\text{CD}_1 \times 10^2$  and  $\text{CD}_2 \times 10^4$ , Normal Consistency (NC) and the F-Score (FS) based on Euclidean distance. We detail their expressions in the supplementary material.

### 4.3. Datasets

**ShapeNet** [12] is used to evaluate object level reconstruction. It consists of various instances of 13 different object classes. We train/test on this dataset using input point clouds of sizes 300 and 3000, and noises of standard deviation ( $\sigma$ ) 0.005 and 0.025. **Synthetic Rooms** [54] is used to evaluate scene level reconstruction. Numerical and qualitative results for this dataset are shown in the supplementary material. It consists of 5000 scenes made of a floor and walls and populated with ShapeNet objects. We train/test on this dataset using inputs of size 10k and a noise of standard deviation 0.005. For both datasets, we follow the train/test

	$\sigma = 0.005$				$\sigma = 0.025$			
	CD <sub>1</sub> ↓	CD <sub>2</sub> ↓	NC ↑	FS ↑	CD <sub>1</sub> ↓	CD <sub>2</sub> ↓	NC ↑	FS ↑
SAP [55]	0.58	1.04	0.89	0.87	1.02	3.50	<b>0.85</b>	<b>0.69</b>
POCO [7]	0.59	1.54	0.88	0.88	1.10	4.40	0.83	0.66
Ours w/o den.	0.55	<b>0.92</b>	0.89	<b>0.89</b>	1.05	3.56	0.84	0.66
Ours	<b>0.54</b>	0.94	<b>0.90</b>	<b>0.89</b>	<b>1.00</b>	<b>3.49</b>	<b>0.85</b>	<b>0.69</b>

Table 1. ShapeNet reconstruction from 300 noisy points, with standard deviations ( $\sigma$ ) of 0.005 and 0.025.

	$\sigma = 0.005$				$\sigma = 0.025$			
	CD <sub>1</sub> ↓	CD <sub>2</sub> ↓	NC ↑	FS ↑	CD <sub>1</sub> ↓	CD <sub>2</sub> ↓	NC ↑	FS ↑
SPR [33]	2.98	-	0.77	0.61	4.99	-	0.60	0.32
3D-R2N2 [18]	1.72	-	0.71	0.40	1.72	-	0.71	0.42
AtlasNet [27]	0.93	-	0.85	0.71	1.17	-	0.82	0.53
ConvONet [54]	0.44	-	0.94	0.94	0.66	-	<b>0.91</b>	0.85
SAP [55]	0.34	0.60	0.94	0.97	<b>0.55</b>	0.95	<b>0.91</b>	<b>0.89</b>
POCO [7]	0.30	0.31	<b>0.95</b>	0.98	0.58	1.24	0.90	0.88
Ours w/o den.	0.32	0.25	0.94	0.98	0.58	0.98	0.90	0.87
Ours	<b>0.29</b>	<b>0.15</b>	<b>0.95</b>	<b>0.99</b>	<b>0.55</b>	<b>0.93</b>	<b>0.91</b>	<b>0.89</b>

Table 2. ShapeNet reconstruction from 3000 noisy points, with standard deviations ( $\sigma$ ) of 0.005 and 0.025.

splits, the training procedure and the evaluation protocol in [7]. Finally, we test the ShapeNet trained models on real scan datasets to evaluate generalization. We use the **FAUST** [6] dataset. It consists of real scans of 10 human body identities in 10 different poses. We sample 3000 points from the scans as inputs. We use the provided mesh registrations to compute IoU. We also use the **ScanNet v2** [19] dataset. It contains 1513 rooms captured with an RGB-D camera. We sample 10k points as inputs.

#### 4.4. Object level reconstruction

Table 1 shows numerical evaluations of ShapeNet [12] reconstructions from 300 noisy input points, with both noises of 0.005 and 0.025 standard deviation. Table 2 shows results for 3000 points with the same noises. We show numbers for our method (Ours) and our method without denoising (Ours w/o denois.). We report numbers for [55] (SAP) and [7] (POCO) using their available models when applicable, and train the rest when needed following their official implementations. We compile numbers for [54] (ConvONet), [33] (SPR), [18] (3D-R2N2), [27] (AtlasNet), from [7, 55]. Figures 4 and 5 show visual comparisons of reconstructions from 3000 points with noises of 0.005 and 0.025 respectively.

Our method outperforms the state-of-the-art across all metrics, and the gap increases overall with input sparsity and noise variance. Using denoising allows us in particular to improve our performance w.r.t. to our baseline especially in the most extreme case (sparse inputs and big variance noise). We note that our denoising-free baseline already achieves mostly on par results with the state-of-

	CD <sub>1</sub> ↓	NC ↑	FS ↑
SA-ConvONet [70]	0.56	0.93	0.92
Neural-Pull [44]	0.71	0.85	0.83
Ours	<b>0.30</b>	<b>0.96</b>	<b>0.99</b>

Table 3. Comparison to test-time fitting methods on class Tables of ShapeNet. Reconstruction from 3000 noisy (0.005 standard deviation) points.

	CD <sub>1</sub> ↓	CD <sub>2</sub> ↓	NC ↑	FS ↑
SAP [55]	0.29	0.13	0.95	0.98
POCO [7]	0.25	0.09	<b>0.96</b>	<b>0.99</b>
Ours	<b>0.23</b>	<b>0.08</b>	<b>0.96</b>	<b>0.99</b>

Table 4. FAUST reconstruction from 3000 points.

the-art method POCO, while using only half the number of parameters (Ours 6.5M, POCO 12.5M). Poisson reconstruction (SPR) is outperformed by learning based methods. Qualitative results show that our method recovers fine structures and details with more fidelity (Figure 4), and that it can perform robustly even under heavy noise (Figure 5), thanks to the combination of local and global reasoning at the decoder, and the denoising of the decoder’s support.

Although they offer mostly superior performance, we note that intrinsic models such as POCO and ours are less parameter efficient than extrinsic ones (*e.g.* ConvONet and SAP contain about 2M parameters). While SAP offers a good model size/performance combination, it is however limited to small scenes by design. We note additionally that our reconstruction time at resolution 128<sup>3</sup> is 538ms (POCO: 1300ms, SAP: 64ms, ConvONet: 381ms).

In Table 3, we compare our feed-forward generalizable method to deep learning optimization based approaches using their official implementations, specifically fitting an MLP to the input point cloud as in Neural-Pull [44], and finetuning ConvONet: SA-ConvONet [70]. As optimization methods are time consuming, we follow here the split of Class Tables in [81]. Our method outperforms these competing methods.

#### 4.5. Object to Real Articulated Shape Generalization

To assess the capacity of our model to generalize outside the training shape distribution (ShapeNet), as well as to reconstruct from real scans, we task the ShapeNet trained model with reconstructing FAUST models from 3000 points. Table 4 shows numerical comparisons using the real scans, with qualitative comparisons displayed in Figure 6. We report numbers for POCO and SAP using their available ShapeNet models. While all presented methods generalize relatively successfully despite not being trained on any articulated shapes, we outperform state-of-the-art methods

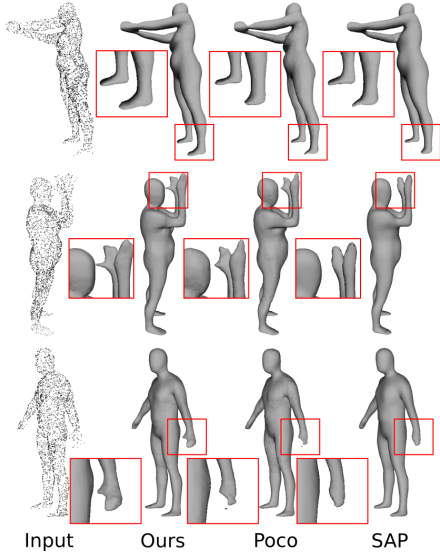


Figure 6. FAUST reconstructions from real 3000 scan points. Models are **trained on ShapeNet**, and they were **not trained on any human or articulated shapes**.

	CD <sub>1</sub> ↓	FS ↑
ConvONet [54]	0.77	0.89
SAP [55]	1.11	0.71
POCO [7]	1.03	0.72
Ours w/o denois.	0.69	0.86
Ours	<b>0.58</b>	<b>0.91</b>

Table 5. ScanNet reconstructions from 10k points.

POCO and SAP on most metrics.

#### 4.6. Object to Real Scenes Generalization

We extend generalization experiments to a more challenging scenario. We use both our’s, SAP’s and POCO’s ShapeNet models trained with 3k sized inputs to reconstruct the real scans of ScanNet [19] using 10k sized inputs. We report results for ConvONet from their paper as a reference point. Table 5 shows numerical results where we outperform the competition. Figure 7 shows a qualitative comparison. We note that as the ConvONet model we show was trained on the Synthetic Rooms dataset using 10k inputs, it tends to produce more flat and extrapolated planar surfaces. Although trained only on objects, our model displays satisfactory scene generalization. We notice also that it tends to be more faithful to the input. These results raise the question of extrapolation vs. input fidelity trade-off desired from reconstruction models, which we would like to explore in future work.

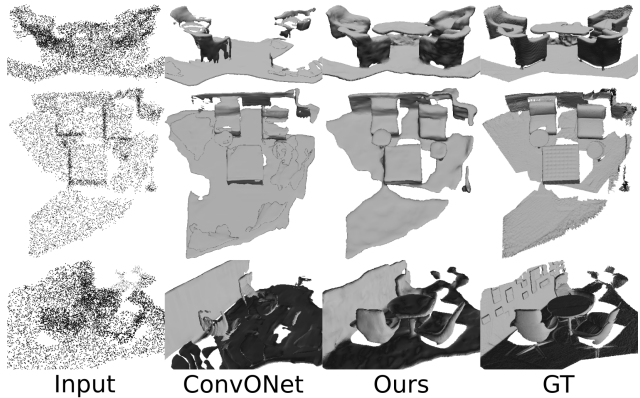


Figure 7. ScanNet reconstructions from real 10k depth sensor points.

	CD <sub>1</sub> ↓	CD <sub>2</sub> ↓	NC ↑	FS ↑
POCO [7]	0.36	0.23	0.95	0.97
Ours w/o den. w/o glob.	0.34	0.23	0.96	0.98
Ours w/o den.	0.33	0.19	0.96	0.98
Ours	<b>0.31</b>	<b>0.14</b>	<b>0.97</b>	<b>0.99</b>

Table 6. Ablation on class Tables of ShapeNet. Reconstruction from 3000 noisy (0.005 std. dev.) points.

#### 4.7. Ablation

We propose a quantitative analysis of the impact of the components of our method at this junction on class Tables of ShapeNet. Results are summarized in Table 6. Starting from our full method (Ours), we ablate denoising (Ours w/o den.) then the global decoding (Ours w/o den. w/o glob.). We also show numbers for POCO. The global decoder helps robustify the method especially against outliers as witnessed by the improvement in L2 chamfer distance when the global mixing is introduced. Denoising improves performance consistently across all metrics as also confirmed in the previous experiments.

#### 5. Conclusion

We showed in this work that coupling denoising with reconstruction is beneficial for intrinsic implicit feed forward reconstruction models. We also showed that for these types of models, a fully MLP based architecture can produce state-of-the-art results with less parameters compared to a convolutional counterpart. This result questions the utility of convolution based locality mechanisms in this context.

#### References

- [1] Nina Amenta, Sunghee Choi, and Ravi Krishna Koluri. The power crust, unions of balls, and the medial axis transform. *CG*, 2001. 3



- [2] Matan Atzmon and Yaron Lipman. Sal: Sign agnostic learning of shapes from raw data. In *CVPR*, 2020. 3
- [3] Matan Atzmon and Yaron Lipman. Sald: Sign agnostic learning with derivatives. In *ICML*, 2020. 3
- [4] Yizhak Ben-Shabat, Chamin Hwa Koneputugodage, and Stephen Gould. Digs: Divergence guided shape implicit neural representation for unoriented point clouds. In *Proceedings of the IEEE/CVF Conference on Computer Vision and Pattern Recognition*, pages 19323–19332, 2022. 3
- [5] Fausto Bernardini, Joshua Mittleman, Holly Rushmeier, Claudio Silva, and Gabriel Taubin. The ball-pivoting algorithm for surface reconstruction. *TVCG*, 1999. 3
- [6] Federica Bogo, Javier Romero, Matthew Loper, and Michael J. Black. FAUST: Dataset and evaluation for 3D mesh registration. In *CVPR*, 2014. 7
- [7] Alexandre Boulch and Renaud Marlet. Poco: Point convolution for surface reconstruction. In *Proceedings of the IEEE/CVF Conference on Computer Vision and Pattern Recognition*, pages 6302–6314, 2022. 1, 2, 3, 4, 5, 6, 7, 8
- [8] Jonathan C Carr, Richard K Beatson, Jon B Cherrie, Tim J Mitchell, W Richard Fright, Bruce C McCallum, and Tim R Evans. Reconstruction and representation of 3d objects with radial basis functions. In *SIGGRAPH*, 2001. 3
- [9] Frédéric Cazals and Joachim Giesen. *Effective Computational Geometry for Curves and Surfaces*. 2006. 3
- [10] Rohan Chabra, Jan E Lenssen, Eddy Ilg, Tanner Schmidt, Julian Straub, Steven Lovegrove, and Richard Newcombe. Deep local shapes: Learning local sdf priors for detailed 3d reconstruction. In *ECCV*, 2020. 3
- [11] Eric R Chan, Connor Z Lin, Matthew A Chan, Koki Nagano, Boxiao Pan, Shalini De Mello, Orazio Gallo, Leonidas J Guibas, Jonathan Tremblay, Sameh Khamis, et al. Efficient geometry-aware 3d generative adversarial networks. In *Proceedings of the IEEE/CVF Conference on Computer Vision and Pattern Recognition*, pages 16123–16133, 2022. 2
- [12] Angel X Chang, Thomas Funkhouser, Leonidas Guibas, Pat Hanrahan, Qixing Huang, Zimo Li, Silvio Savarese, Manolis Savva, Shuran Song, Hao Su, et al. Shapenet: An information-rich 3d model repository. *arXiv preprint arXiv:1512.03012*, 2015. 6, 7, 1
- [13] Zhiqin Chen and Hao Zhang. Learning implicit fields for generative shape modeling. In *CVPR*, 2019. 3
- [14] Zhiqin Chen, Andrea Tagliasacchi, and Hao Zhang. Bsp-net: Generating compact meshes via binary space partitioning. In *Proceedings of the IEEE/CVF Conference on Computer Vision and Pattern Recognition*, 2020. 3
- [15] Julian Chibane and Gerard Pons-Moll. Implicit feature networks for texture completion from partial 3d data. In *European Conference on Computer Vision*, pages 717–725. Springer, 2020. 1, 3
- [16] Julian Chibane, Aymen Mir, and Gerard Pons-Moll. Neural unsigned distance fields for implicit function learning. In *NeurIPS*, 2020. 2, 3
- [17] Jaesung Choe, Chunghyun Park, Francois Rameau, Jaesik Park, and In So Kweon. Pointmixer: Mlp-mixer for point cloud understanding. *arXiv preprint arXiv:2111.11187*, 2021. 1, 2, 4, 5, 6
- [18] Christopher B Choy, Danfei Xu, JunYoung Gwak, Kevin Chen, and Silvio Savarese. 3d-r2n2: A unified approach for single and multi-view 3d object reconstruction. In *ECCV*, 2016. 7
- [19] Angela Dai, Angel X Chang, Manolis Savva, Maciej Halber, Thomas Funkhouser, and Matthias Nießner. Scannet: Richly-annotated 3d reconstructions of indoor scenes. In *Proceedings of the IEEE conference on computer vision and pattern recognition*, pages 5828–5839, 2017. 7, 8
- [20] Boyang Deng, Kyle Genova, Soroosh Yazdani, Sofien Bouaziz, Geoffrey Hinton, and Andrea Tagliasacchi. Cvxnet: Learnable convex decomposition. In *CVPR*, 2020. 3
- [21] Theo Deprelle, Thibault Groueix, Matthew Fisher, Vladimir G Kim, Bryan C Russell, and Mathieu Aubry. Learning elementary structures for 3d shape generation and matching. In *NeurIPS*, 2019. 2
- [22] Philipp Erler, Paul Guerrero, Stefan Ohrhallinger, Niloy J Mitra, and Michael Wimmer. Points2surf learning implicit surfaces from point clouds. In *ECCV*, 2020. 2, 3
- [23] Haoqiang Fan, Hao Su, and Leonidas J Guibas. A point set generation network for 3d object reconstruction from a single image. In *CVPR*, 2017. 2
- [24] Kyle Genova, Forrester Cole, Daniel Vlasic, Aaron Sarna, William T Freeman, and Thomas Funkhouser. Learning shape templates with structured implicit functions. In *ICCV*, 2019. 2
- [25] Kyle Genova, Forrester Cole, Avneesh Sud, Aaron Sarna, and Thomas Funkhouser. Local deep implicit functions for 3d shape. In *CVPR*, 2020. 3
- [26] Amos Gropp, Lior Yariv, Niv Haim, Matan Atzmon, and Yaron Lipman. Implicit geometric regularization for learning shapes. In *ICML*, 2020. 3
- [27] Thibault Groueix, Matthew Fisher, Vladimir G Kim, Bryan C Russell, and Mathieu Aubry. A papier-mâché approach to learning 3d surface generation. In *CVPR*, 2018. 2, 7

- [28] Gaël Guennebaud and Markus Gross. Algebraic point set surfaces. In *ACM siggraph 2007 papers*, pages 23–es. 2007. 1, 3
- [29] John C Hart. Sphere tracing: A geometric method for the antialiased ray tracing of implicit surfaces. *The Visual Computer*, 1996. 2
- [30] Ajay Jain, Ben Mildenhall, Jonathan T. Barron, Pieter Abbeel, and Ben Poole. Zero-shot text-guided object generation with dream fields. 2022. 2
- [31] Chiyu Jiang, Avneesh Sud, Ameesh Makadia, Jingwei Huang, Matthias Nießner, Thomas Funkhouser, et al. Local implicit grid representations for 3d scenes. In *CVPR*, 2020. 3
- [32] Hiroharu Kato, Yoshitaka Ushiku, and Tatsuya Harada. Neural 3d mesh renderer. In *CVPR*, 2018. 2
- [33] Michael Kazhdan and Hugues Hoppe. Screened poisson surface reconstruction. *TOG*, 2013. 1, 3, 7, 2
- [34] Ravikrishna Kolluri. Provably good moving least squares. *TALG*, 2008. 3
- [35] Tianyang Li, Xin Wen, Yu-Shen Liu, Hua Su, and Zhizhong Han. Learning deep implicit functions for 3d shapes with dynamic code clouds. In *Proceedings of the IEEE/CVF Conference on Computer Vision and Pattern Recognition*, pages 12840–12850, 2022. 3
- [36] Siyou Lin, Dong Xiao, Zuoqiang Shi, and Bin Wang. Surface reconstruction from point clouds without normals by parametrizing the gauss formula. *ACM Transactions on Graphics*, 42(2):1–19, 2022. 3
- [37] Stefan Lionar, Daniil Emtsev, Dusan Svilarovic, and Songyou Peng. Dynamic plane convolutional occupancy networks. In *Proceedings of the IEEE/CVF Winter Conference on Applications of Computer Vision*, pages 1829–1838, 2021. 3, 2
- [38] Yaron Lipman. Phase transitions, distance functions, and implicit neural representations. In *ICML*, 2021. 3
- [39] Chen Liu, Jimei Yang, Duygu Ceylan, Ersin Yumer, and Yasutaka Furukawa. Planenet: Piece-wise planar reconstruction from a single rgb image. In *CVPR*, 2018. 2
- [40] Hsueh-Ti Derek Liu, Francis Williams, Alec Jacobson, Sanja Fidler, and Or Litany. Learning smooth neural functions via lipschitz regularization. *arXiv preprint arXiv:2202.08345*, 2022. 3
- [41] Minghua Liu, Xiaoshuai Zhang, and Hao Su. Meshing point clouds with predicted intrinsic-extrinsic ratio guidance. In *ECCV*, 2020. 3
- [42] Shi-Lin Liu, Hao-Xiang Guo, Hao Pan, Peng-Shuai Wang, Xin Tong, and Yang Liu. Deep implicit moving least-squares functions for 3d reconstruction. In *CVPR*, 2021. 3
- [43] William E Lorensen and Harvey E Cline. Marching cubes: A high resolution 3d surface construction algorithm. In *SIGGRAPH*, 1987. 2, 3
- [44] Baorui Ma, Zhizhong Han, Yu-Shen Liu, and Matthias Zwicker. Neural-pull: Learning signed distance functions from point clouds by learning to pull space onto surfaces. In *ICML*, 2021. 3, 7
- [45] Baorui Ma, Yu-Shen Liu, and Zhizhong Han. Reconstructing surfaces for sparse point clouds with on-surface priors. In *Proceedings of the IEEE/CVF Conference on Computer Vision and Pattern Recognition*, pages 6315–6325, 2022. 3
- [46] Baorui Ma, Yu-Shen Liu, Matthias Zwicker, and Zhizhong Han. Surface reconstruction from point clouds by learning predictive context priors. In *Proceedings of the IEEE/CVF Conference on Computer Vision and Pattern Recognition*, pages 6326–6337, 2022. 3
- [47] Corentin Mercier, Thibault Lescoat, Pierre Roussillon, Tamy Boubekeur, and Jean-Marc Thiery. Moving level-of-detail surfaces. *ACM Transactions on Graphics (TOG)*, 41(4):1–10, 2022. 3
- [48] Lars Mescheder, Michael Oechsle, Michael Niemeyer, Sebastian Nowozin, and Andreas Geiger. Occupancy networks: Learning 3d reconstruction in function space. In *Proceedings of the IEEE/CVF conference on computer vision and pattern recognition*, pages 4460–4470, 2019. 2, 3, 6, 1
- [49] Ben Mildenhall, Pratul P Srinivasan, Matthew Tancik, Jonathan T Barron, Ravi Ramamoorthi, and Ren Ng. Nerf: Representing scenes as neural radiance fields for view synthesis. In *ECCV*, 2020. 2
- [50] Amine Ouasfi and Adnane Boukhayma. Few’zero level set’-shot learning of shape signed distance functions in feature space. In *ECCV*, 2022. 3
- [51] Amine Ouasfi and Adnane Boukhayma. Robustifying generalizable implicit shape networks with a tunable non-parametric model. In *NeurIPS*, 2023. 3
- [52] David Palmer, Dmitriy Smirnov, Stephanie Wang, Albert Chern, and Justin Solomon. Deepcurrents: Learning implicit representations of shapes with boundaries. In *Proceedings of the IEEE/CVF Conference on Computer Vision and Pattern Recognition*, pages 18665–18675, 2022. 3
- [53] Jeong Joon Park, Peter Florence, Julian Straub, Richard Newcombe, and Steven Lovegrove. DeepSDF: Learning continuous signed distance functions for shape representation. In *CVPR*, 2019. 2, 3
- [54] Songyou Peng, Michael Niemeyer, Lars Mescheder, Marc Pollefeys, and Andreas Geiger. Convolutional occupancy networks. In *European Conference on Computer Vision*, pages 523–540. Springer, 2020. 1, 2, 3, 6, 7, 8

- [55] Songyou Peng, Chiyu Jiang, Yiyi Liao, Michael Niemeyer, Marc Pollefeys, and Andreas Geiger. Shape as points: A differentiable poisson solver. *Advances in Neural Information Processing Systems*, 34:13032–13044, 2021. 1, 3, 7, 8
- [56] Charles R Qi, Hao Su, Kaichun Mo, and Leonidas J Guibas. Pointnet: Deep learning on point sets for 3d classification and segmentation. In *CVPR*, 2017. 3
- [57] Charles Ruizhongtai Qi, Li Yi, Hao Su, and Leonidas J Guibas. Pointnet++: Deep hierarchical feature learning on point sets in a metric space. *Advances in neural information processing systems*, 30, 2017. 4
- [58] Marie-Julie Rakotosaona, Vittorio La Barbera, Paul Guerrero, Niloy J Mitra, and Maks Ovsjanikov. Pointcleanet: Learning to denoise and remove outliers from dense point clouds. In *Computer Graphics Forum*, pages 185–203. Wiley Online Library, 2020. 6
- [59] Marie-Julie Rakotosaona, Noam Aigerman, Niloy Mitra, Maks Ovsjanikov, and Paul Guerrero. Differentiable surface triangulation. In *SIGGRAPH Asia*, 2021. 3
- [60] Gernot Riegler, Ali Osman Ulusoy, and Andreas Geiger. Octnet: Learning deep 3d representations at high resolutions. In *CVPR*, 2017. 2
- [61] Olaf Ronneberger, Philipp Fischer, and Thomas Brox. U-net: Convolutional networks for biomedical image segmentation. In *International Conference on Medical image computing and computer-assisted intervention*, pages 234–241. Springer, 2015. 4
- [62] Bernhard Schölkopf, Joachim Giesen, and Simon Spalinger. Kernel methods for implicit surface modeling. In *NeurIPS*, 2004. 3
- [63] Johannes Lutz Schönberger and Jan-Michael Frahm. Structure-from-motion revisited. In *Conference on Computer Vision and Pattern Recognition (CVPR)*, 2016. 1
- [64] Johannes Lutz Schönberger, Enliang Zheng, Marc Pollefeys, and Jan-Michael Frahm. Pixelwise view selection for unstructured multi-view stereo. In *European Conference on Computer Vision (ECCV)*, 2016. 1
- [65] Vincent Sitzmann, Michael Zollhoefer, and Gordon Wetzstein. Scene representation networks: Continuous 3d-structure-aware neural scene representations. In *NeurIPS*, 2019. 3
- [66] Vincent Sitzmann, Eric R Chan, Richard Tucker, Noah Snavely, and Gordon Wetzstein. Metasdf: Meta-learning signed distance functions. In *NeurIPS*, 2020. 3
- [67] Vincent Sitzmann, Julien Martel, Alexander Bergman, David Lindell, and Gordon Wetzstein. Implicit neural representations with periodic activation functions. In *NeurIPS*, 2020. 3
- [68] Vincent Sitzmann, Semon Rezkikov, William T Freeman, Joshua B Tenenbaum, and Fredo Durand. Light field networks: Neural scene representations with single-evaluation rendering. In *NeurIPS*, 2021. 3
- [69] Towaki Takikawa, Joey Litalien, Kangxue Yin, Karsten Kreis, Charles Loop, Derek Nowrouzezahrai, Alec Jacobson, Morgan McGuire, and Sanja Fidler. Neural geometric level of detail: Real-time rendering with implicit 3d shapes. In *CVPR*, 2021. 3
- [70] Jiapeng Tang, Jiabao Lei, Dan Xu, Feiying Ma, Kui Jia, and Lei Zhang. Sa-convonet: Sign-agnostic optimization of convolutional occupancy networks. In *Proceedings of the IEEE/CVF International Conference on Computer Vision*, pages 6504–6513, 2021. 7
- [71] Maxim Tatarchenko, Alexey Dosovitskiy, and Thomas Brox. Octree generating networks: Efficient convolutional architectures for high-resolution 3d outputs. In *ICCV*, 2017. 2
- [72] Ilya O Tolstikhin, Neil Houlsby, Alexander Kolesnikov, Lucas Beyer, Xiaohua Zhai, Thomas Unterthiner, Jessica Yung, Andreas Steiner, Daniel Keysers, Jakob Uszkoreit, et al. Mlp-mixer: An all-mlp architecture for vision. *Advances in Neural Information Processing Systems*, 34:24261–24272, 2021. 1, 4
- [73] Edgar Tretschk, Ayush Tewari, Vladislav Golyanik, Michael Zollhöfer, Carsten Stoll, and Christian Theobalt. Patchnets: Patch-based generalizable deep implicit 3d shape representations. In *ECCV*, 2020. 3
- [74] Shubham Tulsiani, Hao Su, Leonidas J. Guibas, Alexei A. Efros, and Jitendra Malik. Learning shape abstractions by assembling volumetric primitives. In *CVPR*, 2017. 2
- [75] Rahul Venkatesh, Tejan Karmali, Sarthak Sharma, Aurobrata Ghosh, R Venkatesh Babu, László A Jeni, and Maneesh Singh. Deep implicit surface point prediction networks. In *CVPR*, 2021. 3
- [76] Nanyang Wang, Yinda Zhang, Zhuwen Li, Yanwei Fu, Wei Liu, and Yu-Gang Jiang. Pixel2mesh: Generating 3d mesh models from single rgb images. In *ECCV*, 2018. 2
- [77] Peng Wang, Lingjie Liu, Yuan Liu, Christian Theobalt, Taku Komura, and Wenping Wang. Neus: Learning neural implicit surfaces by volume rendering for multi-view reconstruction. *arXiv preprint arXiv:2106.10689*, 2021. 2
- [78] Peng-Shuai Wang, Yang Liu, Yu-Xiao Guo, Chun-Yu Sun, and Xin Tong. O-cnn: Octree-based convolutional neural networks for 3d shape analysis. *TOG*, 2017. 2
- [79] Shaofei Wang, Marko Mihajlovic, Qianli Ma, Andreas Geiger, and Siyu Tang. Metaavatar: Learning animatable clothed human models from few depth images.

- Advances in Neural Information Processing Systems*, 34:2810–2822, 2021. 3
- [80] Francis Williams, Teseo Schneider, Claudio Silva, Denis Zorin, Joan Bruna, and Daniele Panozzo. Deep geometric prior for surface reconstruction. In *CVPR*, 2019. 2
- [81] Francis Williams, Matthew Trager, Joan Bruna, and Denis Zorin. Neural splines: Fitting 3d surfaces with infinitely-wide neural networks. In *CVPR*, 2021. 3, 7
- [82] Francis Williams, Zan Gojcic, Sameh Khamis, Denis Zorin, Joan Bruna, Sanja Fidler, and Or Litany. Neural fields as learnable kernels for 3d reconstruction. In *CVPR*, 2022. 3
- [83] Sanghyun Woo, Jongchan Park, Joon-Young Lee, and In So Kweon. Cbam: Convolutional block attention module. In *Proceedings of the European conference on computer vision (ECCV)*, pages 3–19, 2018. 5
- [84] Jiajun Wu, Chengkai Zhang, Tianfan Xue, William T Freeman, and Joshua B Tenenbaum. Learning a probabilistic latent space of object shapes via 3d generative-adversarial modeling. In *NeurIPS*, 2016. 2
- [85] Zhirong Wu, Shuran Song, Aditya Khosla, Fisher Yu, Linguang Zhang, Xiaoou Tang, and Jianxiong Xiao. 3d shapenets: A deep representation for volumetric shapes. In *CVPR*, 2015. 2
- [86] Lior Yariv, Jiatao Gu, Yoni Kasten, and Yaron Lipman. Volume rendering of neural implicit surfaces. *Advances in Neural Information Processing Systems*, 34:4805–4815, 2021. 2
- [87] Mohsen Yavartanoo, Jaeyoung Chung, Reyhaneh Neshatavar, and Kyoung Mu Lee. 3dias: 3d shape reconstruction with implicit algebraic surfaces. In *ICCV*, 2021. 3
- [88] Jianglong Ye, Yuntao Chen, Naiyan Wang, and Xiao-long Wang. Gifs: Neural implicit function for general shape representation. In *Proceedings of the IEEE/CVF Conference on Computer Vision and Pattern Recognition*, pages 12829–12839, 2022. 3
- [89] Hengshuang Zhao, Li Jiang, Chi-Wing Fu, and Jiaya Jia. Pointweb: Enhancing local neighborhood features for point cloud processing. In *Proceedings of the IEEE/CVF conference on computer vision and pattern recognition*, pages 5565–5573, 2019. 4
- [90] Hengshuang Zhao, Li Jiang, Jiaya Jia, Philip HS Torr, and Vladlen Koltun. Point transformer. In *Proceedings of the IEEE/CVF International Conference on Computer Vision*, pages 16259–16268, 2021. 4
- [91] Junsheng Zhou, Baorui Ma, Liu Yu-Shen, Fang Yi, and Han Zhizhong. Learning consistency-aware unsigned distance functions progressively from raw point clouds. In *Advances in Neural Information Processing Systems (NeurIPS)*, 2022. 2
- [92] Chuhan Zou, Ersin Yumer, Jimei Yang, Duygu Ceylan, and Derek Hoiem. 3d-prnn: Generating shape primitives with recurrent neural networks. In *CVPR*, 2017. 2



# Mixing-Denoising Generalizable Occupancy Networks

## Supplementary Material

### 6. Evaluation metrics

Following the definitions from [7], we present, in this section, the formal definitions for the metrics that we use for evaluation. We denote by  $\mathcal{S}$  and  $\hat{\mathcal{S}}$  the ground truth and predicted mesh respectively. All metrics are approximated with 100k samples from  $\mathcal{S}$  and  $\hat{\mathcal{S}}$ .

**Chamfer distance** We provide two variations of the Chamfer distance using the two-ways nearest neighbor distance and squared distance, respectively:

$$CD_1 = \frac{1}{2|\mathcal{S}|} \sum_{v \in \mathcal{S}} \min_{\hat{v} \in \hat{\mathcal{S}}} \|v - \hat{v}\|_2 + \frac{1}{2|\hat{\mathcal{S}}|} \sum_{\hat{v} \in \hat{\mathcal{S}}} \min_{v \in \mathcal{S}} \|\hat{v} - v\|_2$$

$$CD_2 = \frac{1}{2|\mathcal{S}|} \sum_{v \in \mathcal{S}} \min_{\hat{v} \in \hat{\mathcal{S}}} \|v - \hat{v}\|_2^2 + \frac{1}{2|\hat{\mathcal{S}}|} \sum_{\hat{v} \in \hat{\mathcal{S}}} \min_{v \in \mathcal{S}} \|\hat{v} - v\|_2^2$$

**F-Score (FS)** For a given threshold  $\tau$ , the F-score between the meshes  $\mathcal{S}$  and  $\hat{\mathcal{S}}$  is defined as:

$$FS(\tau, \mathcal{S}, \hat{\mathcal{S}}) = \frac{2 \text{ Recall} \cdot \text{ Precision}}{\text{ Recall} + \text{ Precision}}$$

where

$$\text{Recall}(\tau, \mathcal{S}, \hat{\mathcal{S}}) = |\{v \in \mathcal{S}, \text{ s.t. } \min_{\hat{v} \in \hat{\mathcal{S}}} \|v - \hat{v}\|_2 < \tau\}|$$

$$\text{Precision}(\tau, \mathcal{S}, \hat{\mathcal{S}}) = |\{\hat{v} \in \hat{\mathcal{S}}, \text{ s.t. } \min_{v \in \mathcal{S}} \|v - \hat{v}\|_2 < \tau\}|$$

Following ONet [48] and ConvONet [54], we set  $\tau$  to 0.01.

**Normal consistency (NC)** We denote here by  $n_v$  the normal at a point  $v$  in  $\mathcal{S}$ . The normal consistency between two meshes  $\mathcal{S}$  and  $\hat{\mathcal{S}}$  is defined as:

$$NC = \frac{1}{2|\mathcal{S}|} \sum_{v \in \mathcal{S}} n_v \cdot n_{\text{closest}(v, \hat{\mathcal{S}})} + \frac{1}{2|\hat{\mathcal{S}}|} \sum_{\hat{v} \in \hat{\mathcal{S}}} n_{\hat{v}} \cdot n_{\text{closest}(\hat{v}, \mathcal{S})}$$

where

$$\text{closest}(v, \hat{\mathcal{S}}) = \text{argmin}_{\hat{v} \in \hat{\mathcal{S}}} \|v - \hat{v}\|_2$$

### 7. Additional Object Reconstruction Numerical Results

We report our per class ShapeNet[12] reconstruction results from 3000 noisy points in Table 7, and 300 noisy points in Table 8. We show numbers for both noises of 0.005 and 0.025 standard deviation.

	$\sigma = 0.005$		$\sigma = 0.025$	
	CD <sub>1</sub> ↓	CD <sub>2</sub> ↓	CD <sub>1</sub> ↓	CD <sub>2</sub> ↓
Airplane	0.23	0.08	0.48	0.42
Bench	0.29	0.12	0.52	0.51
Cabinet	0.35	0.19	0.56	0.91
Car	0.39	0.31	0.78	1.62
Chair	0.34	0.17	0.60	0.73
Display	0.29	0.12	0.49	0.43
Lamp	0.29	0.19	0.71	3.90
Speaker	0.40	0.32	0.67	1.18
Rifle	0.19	0.05	0.44	0.37
Sofa	0.30	0.14	0.53	0.56
Table	0.31	0.14	0.50	0.59
Phone	0.23	0.07	0.36	0.22
Vessel	0.25	0.10	0.57	0.68

Table 7. ShapeNet reconstruction from 3000 noisy points, with standard deviations ( $\sigma$ ) of 0.005 and 0.025.

	$\sigma = 0.005$		$\sigma = 0.025$	
	CD <sub>1</sub> ↓	CD <sub>2</sub> ↓	CD <sub>1</sub> ↓	CD <sub>2</sub> ↓
Airplane	0.45	0.45	0.89	1.88
Bench	0.50	0.56	0.97	2.70
Cabinet	0.56	0.88	0.95	2.26
Car	0.83	2.02	1.21	3.20
Chair	0.62	0.97	1.21	5.50
Display	0.48	0.54	0.89	1.63
Lamp	0.67	2.32	1.39	14.17
Speaker	0.75	2.03	1.26	4.34
Rifle	0.36	0.26	0.72	1.17
Sofa	0.52	0.64	1.00	2.09
Table	0.52	0.75	0.95	3.21
Phone	0.34	0.21	0.63	0.78
Vessel	0.51	0.61	1.03	2.40

Table 8. ShapeNet reconstruction from 300 noisy points, with standard deviations ( $\sigma$ ) of 0.005 and 0.025.

### 8. Additional Object Reconstruction Qualitative Results

We show additional ShapeNet[12] reconstructions using our method from 3000 noisy points with noise standard deviation 0.005 in Figure 8. We show the input point cloud, our denoised point cloud, and the output mesh.

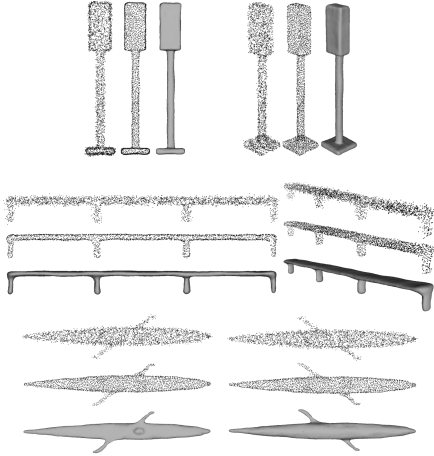


Figure 8. ShapeNet reconstructions from 3000 noisy (0.005) points. We show the **input** point cloud, our **denoising** and our **reconstruction**.

## 9. Additional Scene Reconstruction Results

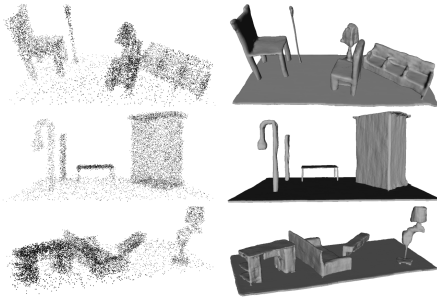


Figure 9. Synthetic Rooms reconstructions from 10k noisy points, with standard deviation of 0.005.

	CD <sub>1</sub> ↓	CD <sub>2</sub> ↓	NC ↑	FS ↑
SPR [33]	2.23	-	0.87	0.81
ONet [48]	2.03	-	0.78	0.54
DP-ConvONet [37]	0.42	-	0.91	0.96
ConvONet [54]	0.42	-	0.91	0.96
POCO [7]	<b>0.36</b>	0.31	<b>0.92</b>	<b>0.98</b>
Ours w/o den.	0.38	0.29	0.90	0.97
Ours	<b>0.36</b>	<b>0.25</b>	0.91	<b>0.98</b>

Table 9. Synthetic Rooms reconstruction from 10k noisy points, with standard deviation of 0.005. **POCO: 12.5M params./ Ours: 6.5M params.**

Table 9 shows numerical evaluations of Synthetic Rooms [54] reconstructions from 10k points with 0.005 standard deviation noise. We report numbers for POCO using their available model and we compile numbers for ConvONet

[54], DP-ConvONet [37], SPR [33], ONet [48] from [7]. Figure 9 shows a few reconstruction examples. We perform overall on par with POCO on this task, while achieving a lower L2 Chamfer score, which we believe is on account of our global decoder and denoising. We pinpoint again that we are working with only half the model size of POCO (6.5M vs. 12.5M).